HAL
open science

Constraining the Date of the Martian Dynamo Shutdown by Means of Crater Magnetization Signatures

Foteini Vervelidou, Vincent Lesur, Matthias Grott, Achim Morschhauser, Robert J. Lillis

To cite this version:

Foteini Vervelidou, Vincent Lesur, Matthias Grott, Achim Morschhauser, Robert J. Lillis. Constraining the Date of the Martian Dynamo Shutdown by Means of Crater Magnetization Signatures. Journal of Geophysical Research. Planets, 2017, 122, pp.2294-2311. 10.1002/2017JE005410 . insu-03748827

HAL Id: insu-03748827

https://insu.hal.science/insu-03748827v1

Submitted on 10 Aug 2022

HAL is a multi-disciplinary open access archive for the deposit and dissemination of scientific research documents, whether they are published or not. The documents may come from teaching and research institutions in France or abroad, or from public or private research centers.

L'archive ouverte pluridisciplinaire **HAL**, est destinée au dépôt et à la diffusion de documents scientifiques de niveau recherche, publiés ou non, émanant des établissements d'enseignement et de recherche français ou étrangers, des laboratoires publics ou privés.

Copyright

AGU PUBLICATIONS

JGR

Journal of Geophysical Research: Planets

RESEARCH ARTICLE

10.1002/2017JE005410

Key Points:
- A visible magnetization model of Mars is obtained up to SH degree and order 110
- A zero visible magnetization is shown to be a valid proxy for a crater's entire magnetization being zero in the absence of major alterations
- The Martian dynamo ceased during the Noachian era

Supporting Information:
- Supporting Information S1

Correspondence to:
F. Vervelidou,
foteini@gfz-potsdam.de

Citation:
Vervelidou, F., Lesur, V., Grott, M., Morschhauser, A., & Lillis, R. J. (2017). Constraining the date of the Martian dynamo shutdown by means of crater magnetization signatures. *Journal of Geophysical Research: Planets*, *122*, 2294–2311. https://doi.org/10.1002/2017JE005410

Received 2 AUG 2017
Accepted 3 OCT 2017
Accepted article online 9 OCT 2017
Published online 11 NOV 2017

©2017. American Geophysical Union. All Rights Reserved.

Constraining the Date of the Martian Dynamo Shutdown by Means of Crater Magnetization Signatures

Foteini Vervelidou[1], Vincent Lesur[2], Matthias Grott[3], Achim Morschhauser[1], and Robert J. Lillis[4]

[1]Helmholtz Centre Potsdam-GFZ German Research Centre for Geosciences, Section 2.3 Earth's magnetic field, Potsdam, Germany, [2]Equipe de géomagnétisme, Institut de Physique du Globe de Paris, Paris, France, [3]Department of Planetary Physics, Institute of Planetary Research, German Aerospace Center, Berlin, Germany, [4]UC Berkeley Space Sciences Laboratory, Oakland, CA, USA

Abstract Mars is believed to have possessed a dynamo that ceased operating approximately 4 Ga ago, although the exact time is still under debate. The scope of this study is to constrain the possible timing of its cessation by studying the magnetization signatures of craters. The study uses the latest available model of the lithospheric magnetic field of Mars, which is based on Mars Global Surveyor data. We tackle the problem of nonuniqueness that characterizes the inversion of magnetic field data for the magnetization by inferring only the visible part of the magnetization, that is, the part of the magnetization that gives rise to the observed magnetic field. Further on, we demonstrate that a zero visible magnetization is a valid proxy for the entire magnetization being zero under the assumption of a magnetization distribution of induced geometry. This assumption holds for craters whose thermoremanent magnetization has not been significantly altered since its acquisition. Our results show that the dynamo shut off after the impacts that created the Acidalia and SE Elysium basins and before the crust within the Utopia basin cooled below its magnetic blocking temperature. Accounting for the age uncertainties in the dating of these craters, we estimate that the dynamo shut off at an *N*(300) crater retention age of 2.5–3.2 or an absolute model age of 4.12–4.14 Ga. Moreover, the Martian dynamo may have been weaker in its early stage, which if true implies that the driving mechanism of the Martian dynamo was not the same throughout its history.

Plain Language Summary Mars is believed to have possessed a dynamo that ceased operating approximately 4 Ga ago, although the exact time is still under debate. The scope of this study is to constrain the possible timing of its cessation by studying the magnetization signatures of craters. The study uses the latest available model of the lithospheric magnetic field of Mars, which is based on Mars Global Surveyor data. Since the complete magnetization cannot be uniquely recovered by magnetic field measurements, we infer the visible part of the magnetization, that is, the part of the magnetization that gives rise to the observed magnetic field. Further on, we demonstrate that a zero visible magnetization is a valid proxy for craters whose thermoremanent magnetization has not been significantly altered since its acquisition. Our results show that the dynamo shut off after the impacts that created the Acidalia and SE Elysium basins and before the crust within the Utopia basin cooled down. Accounting for the age uncertainties in the dating of these craters, we estimate that the dynamo shut off at an absolute model age of 4.12–4.14 Ga. Moreover, the Martian dynamo may have been weaker in its early stage, which if true implies that that the driving mechanism of the Martian dynamo was not the same throughout its history.

1. Introduction

Mars Global Surveyor (MGS) observations revealed that Mars carries a strong crustal magnetic field in the absence of an active core dynamo. The characteristics of this field suggest that it was induced by a core dynamo, which ceased operating at some point in the past (Acuña et al., 2001, Connerney et al., 2001, 2004). The additional observation that the magnetic field signal is very low over large impact craters, like Utopia, Hellas, and Argyre, has been seen as evidence for a dynamo that had already ceased operating when these structures formed (e.g., Acuña et al., 1999; Arkani-Hamed, 2004; Hood et al., 2003; Lillis et al., 2008; Mohit & Arkani-Hamed, 2004).

Due to the high temperature and pressure that arise when an impact takes place, most of the crust of the impact basin gets demagnetized, both laterally and in depth, through excavation, shock, and heating

(see, e.g., Arkani-Hamed, 2005; Lillis, Stewart, et al., 2013; Louzada et al., 2011; Shahnas & Arkani-Hamed, 2007). In the presence of an ambient magnetic field, it gets remagnetized by acquiring thermoremanent magnetization as the affected crust cools below its magnetic blocking temperature. Thermal remagnetization may only affect the crust closer to the crater's center, while the remainder of the crust may be less affected, mainly through excavation and shock demagnetization and remagnetization. Therefore, craters that are not magnetized, especially close to their centers, suggest the absence of an ambient magnetic field. According to this reasoning, the magnetization signature of craters can be used to infer the timeline of the Martian dynamo.

An alternative approach to infer information about the history of the dynamo relies on the magnetization signature of volcanoes. Such an approach has been followed by Langlais and Purucker (2007) who looked at the magnetization signature over Apollinaris Patera and infered that the dynamo was still active past the Noachian era. Similar conclusions were reached by Milbury et al. (2012), who looked at the magnetization signature of Tyrrhenus Mons and Syrtis Major and argued that the dynamo was active during the Hesperian era. Lillis, Robbins, et al. (2013), however, argued that because there is a tenuous connection between the age of the magnetization in the whole depth of crust and the age of the oldest visible surface lava flows, the magnetization signatures of volcanoes are not a reliable tool for dating the dynamo.

Reconstructing the history of the dynamo can lead to a better understanding of the planet's interior as the operation of a dynamo is directly related to the thermal and chemical evolution of the planet (see, e.g., Breuer et al., 2010; Connerney et al., 2004; Stevenson, 2001). The duration over which the dynamo remained active has important implications for the mechanism that sustained it (see, e.g., Schubert et al., 2000). Moreover, in case of Mars, the magnetic field generated by its dynamo might have played a key role in shielding the Martian atmosphere from erosion by the solar wind (e.g., Dehant et al., 2007). Therefore, the study of the dynamo history is crucial also for deciphering past Martian climate.

However, using the magnetic field signal over impact craters to infer the history of the dynamo is not necessarily straightforward. The main uncertainties involve the precision and accuracy of the craters' age determination (see, e.g., Robbins et al., 2013), the existence of a variety of mechanisms that can modify the magnetization signature, like chemical alteration, crustal thinning, or hydrothermal activity (see, e.g., Solomon et al., 2005), and the inherent nonuniqueness in inverting magnetic field measurements to constrain the magnetization. In order to tackle the nonuniqueness issue, Whaler and Purucker (2005) have suggested a magnetization model based on a minimum norm solution. Milbury and Schubert (2010) modeled the source as a layer of constant thickness, partially magnetized by a single inducing dipole. Interested in inferring the dynamo shutoff date from crater magnetization signatures, Lillis et al. (2008, 2010) and Lillis, Robbins, et al. (2013) have opted for a statistical approach assigning a certain probability to a crater being magnetized or demagnetized based on its magnetic field signature, its size, and the coherence scale of its magnetization.

Arkani-Hamed (2002) derived a magnetization model of Mars by deriving equations that link the spherical harmonic (SH) coefficients of the magnetic field to the SH coefficients of the vertically averaged magnetization, under the assumption of a dipolar inducing field. Here we follow a similar approach for inferring the magnetization signatures of craters, but we impose no restrictions on the inducing field, and moreover, we alleviate the nonuniqueness issue by using the vector SH formalism. This formalism allows for partitioning the magnetization into the part that gave rise to the observed magnetic field and the magnetization's null space. We infer only the former and demonstrate that when it comes to characterizing a crater as magnetized or nonmagnetized, this part of the magnetization is a valid proxy under certain assumptions.

The paper is separated into three parts. In section 2 we describe how we obtain our magnetization model and the assumptions under which this can be used to distinguish magnetized from non magnetized craters. The two main derivations of this section are given in the appendix. In section 3 we present our results, and in section 4 we discuss their implications for the history of the Martian dynamo.

2. Data and Methods

2.1. Global Visible Magnetization Model as a Valid Proxy

We base our study on the lithospheric magnetic field model obtained by Morschhauser et al. (2014), and we estimate the magnetization distribution that is necessary to give rise to the magnetic field in this model. This magnetization has been termed the visible part of the magnetization (Vervelidou et al., 2017), as opposed to the null space of the magnetization, which generates a magnetic field that stays trapped inside or below the

sources (see also Gubbins et al., 2011). More precisely, if **M** is the entire magnetization distribution, its decomposition into vector SH gives (see equation (28) of Gubbins et al., 2011 and equations (5)–(8) of Vervelidou et al., 2017)

$$\mathbf{M} = \mathcal{I} + \mathcal{E} + \mathcal{T} \tag{1}$$

with

$$\mathcal{I} = \sum_{l} \sum_{m=0}^{l} g_{\mathcal{I},l}^{m} \mathbf{Y}_{l,l-1}^{m,c} + h_{\mathcal{I},l}^{m} \mathbf{Y}_{l,l-1}^{m,s}, \tag{2}$$

$$\mathcal{E} = \sum_{l} \sum_{m=0}^{l} g_{\mathcal{E},l}^{m} \mathbf{Y}_{l,l+1}^{m,c} + h_{\mathcal{E},l}^{m} \mathbf{Y}_{l,l+1}^{m,s}, \tag{3}$$

and

$$\mathcal{T} = \sum_{l} \sum_{m=0}^{l} g_{\mathcal{T},l}^{m} \mathbf{Y}_{l,l}^{m,c} + h_{\mathcal{T},l}^{m} \mathbf{Y}_{l,l}^{m,s}, \tag{4}$$

where $\mathcal{I}$ stands for the visible part of **M**, the sum $\mathcal{E} + \mathcal{T}$ spans the magnetization's null space, $\left\{g_{\mathcal{I},l}^{m}, h_{\mathcal{I},l}^{m}\right\}$, $\left\{g_{\mathcal{E},l}^{m}, h_{\mathcal{E},l}^{m}\right\}$, and $\left\{g_{\mathcal{T},l}^{m}, h_{\mathcal{T},l}^{m}\right\}$ are the vector spherical harmonic coefficients of order m and degree l of $\mathcal{I}$, $\mathcal{E}$, and $\mathcal{T}$, respectively, and $\left\{\mathbf{Y}_{l,l-1}^{m,c}, \mathbf{Y}_{l,l-1}^{m,s}\right\}$, $\left\{\mathbf{Y}_{l,l+1}^{m,c}, \mathbf{Y}_{l,l+1}^{m,s}\right\}$, and $\left\{\mathbf{Y}_{l,l}^{m,c}, \mathbf{Y}_{l,l}^{m,s}\right\}$ are the three types of real vector spherical harmonics given by

$$\mathbf{Y}_{l,l-1}^{m(c,s)} = \frac{1}{r^{l-1}\sqrt{l(2l+1)}} \nabla \left[r^{l} Y_{l}^{m(c,s)}(\theta,\phi)\right], \tag{5}$$

$$\mathbf{Y}_{l,l+1}^{m(c,s)} = \frac{r^{l+2}}{\sqrt{(l+1)(2l+1)}} \nabla \left[\frac{1}{r^{l+1}} Y_{l}^{m(c,s)}(\theta,\phi)\right], \tag{6}$$

and

$$\mathbf{Y}_{l,l}^{m(c,s)} = -\frac{1}{\sqrt{l(l+1)}} \mathbf{r} \times \nabla Y_{l}^{m(c,s)}(\theta,\phi), \tag{7}$$

with

$$Y_{l}^{m,c} = P_{l}^{m}(\cos\theta)\cos(m\phi), \tag{8}$$

and

$$Y_{l}^{m,s} = P_{l}^{m}(\cos\theta)\sin(m\phi) \tag{9}$$

being the Schmidt seminormalized real spherical harmonics of degree l and order m, whose norm is given by

$$\oint Y_{l}^{m(c,s)} Y_{l'}^{m'(c,s)} \mathrm{d}\Omega = \frac{4\pi}{2l+1} \delta_{ll'} \delta_{mm'} \tag{10}$$

(see also equations (16)–(27) of Gubbins et al., 2011, and equations (A1)–(A6) of Vervelidou et al., 2017).

Gubbins et al. (2011) and Vervelidou et al. (2017) propose formulas that convert the spherical harmonic (SH) coefficients of a given lithospheric magnetic field model, $\left\{g_{l}^{m}, h_{l}^{m}\right\}$, into the vector SH coefficients of the visible part of the magnetization, $\left\{g_{\mathcal{I},l}^{m}, h_{\mathcal{I},l}^{m}\right\}$ (see their equations (32)–(33) and their equation (9), respectively), under the assumption of a magnetized layer of infinitesimal thickness. Here we derive a similar formula that is valid for the case of a magnetized layer of finite thickness, when this is the upper layer of a sphere with radius R, and in which the magnetization varies only laterally. This formula reads (see the appendix for the derivation)

$$\left\{\begin{matrix} g_{\mathcal{I},l}^{m} \\ h_{\mathcal{I},l}^{m} \end{matrix}\right\} = \frac{l+2}{\mu_0}\sqrt{\frac{2l+1}{l}} \frac{1}{\left[1-\left(1-\frac{t}{R}\right)^{l+2}\right]} \left\{\begin{matrix} g_{l}^{m} \\ h_{l}^{m} \end{matrix}\right\}, \tag{11}$$

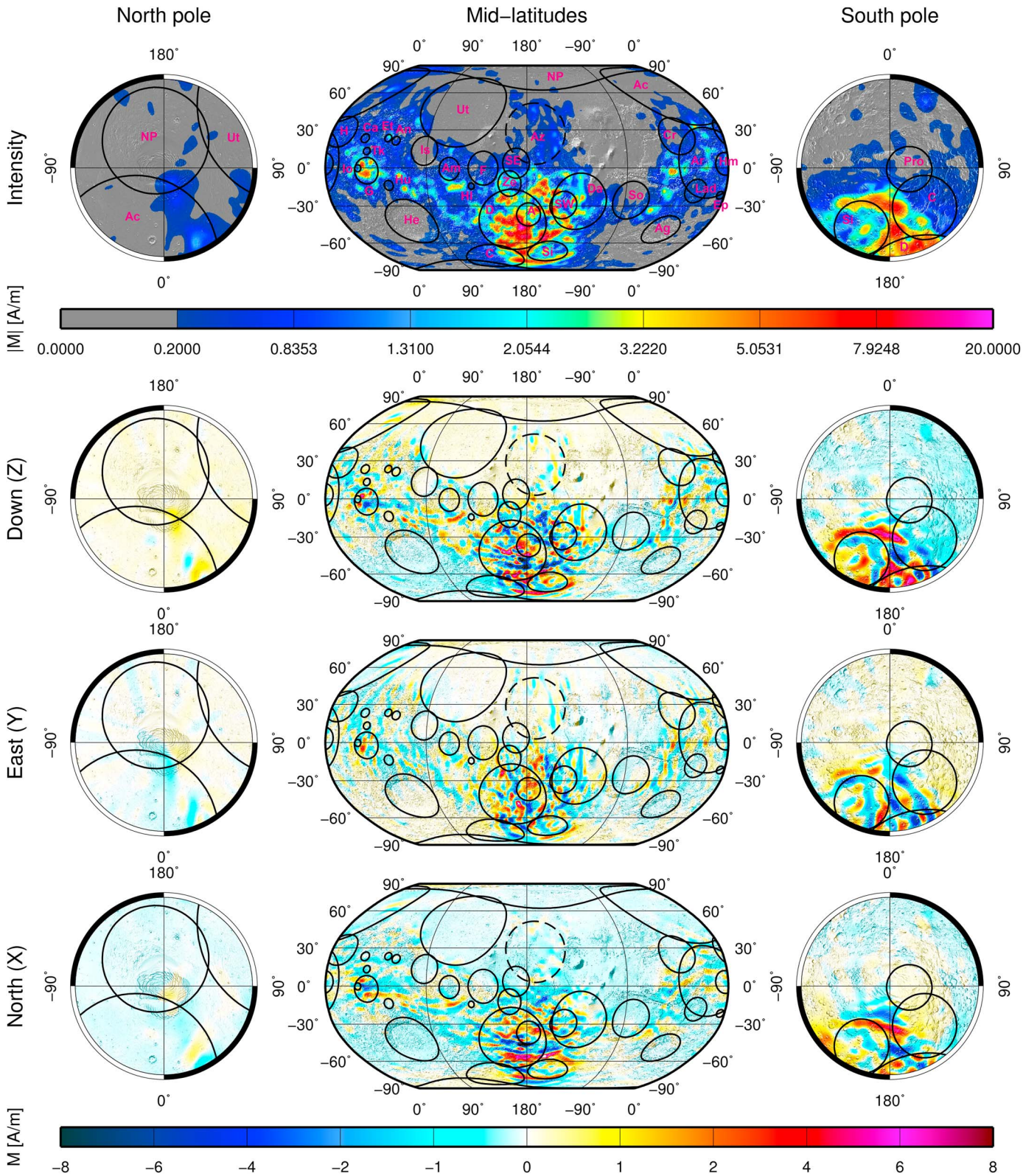

Figure 1. The model of Mars' visible magnetization obtained by means of equation (11) and the SH lithospheric magnetic field model of Morschhauser et al. (2014). The rims of the craters considered in this study are shown together with their abbreviated names (see Table 1 for the full name of the craters). The crater Amazonis (Az) (dashed, black circle) is only shown because of its overlap with the crater SE Elysium (SE) (see text for details). The magnetization intensity, and the *Z*, *Y*, and *X* components are shown (top to bottom). Stereographic projections of the North Pole and South Pole, down to 60° and −60° latitude, respectively, are shown on the left- and right-hand side of the figure, respectively, along with a Robinson projection of all latitudes in the center of the figure.

where μ_0 is the magnetic constant in units of H/m, t is the thickness of the magnetized layer, and R is the radius of the upper spherical surface of the magnetized layer and the reference radius of the SH coefficients of the lithospheric magnetic field model, $\{g_l^m, h_l^m\}$. These coefficients are given in nanotesla and the vector SH coefficients of the visible magnetization, $\left\{g_{\mathcal{I},l}^m, h_{\mathcal{I},l}^m\right\}$, are given in nA/m. Evidently, this conversion formula allows only the recovery of the $\{gl_l^m, hl_l^m\}$ coefficients whose degree and order are smaller than or equal to the maximum degree and order of the lithospheric magnetic field model coefficients, $\{g_l^m, h_l^m\}$. By means of the above formula we convert the lithospheric magnetic field model of Morschhauser et al. (2014) into a visible magnetization model, shown in Figure 1. For this, we consider a magnetic crust that is 40 km thick, in agreement with previous studies (Langlais et al., 2004; Voorhies, 2008; Whaler and Purucker, 2005).

Further on, we focus on craters for which we can assume that a substantial portion of their crust has not undergone significant movements or chemical alterations since they got (de)magnetized and, consequently, the magnetization there remains principally intact since their formation. This is a necessary assumption, made, implicitly or explicitly, by all studies that use magnetization signatures of craters to infer information about the dynamo history. Under this assumption, the craters' magnetization, at least close to their center, is considered to be thermoremanent and therefore to preserve the geometry of the past inducing field. In this case, it can be shown (see Appendix B for the demonstration) that $\mathcal{E}$ is zero if and only if $\mathcal{I}$ is zero, and vice versa. In other words, if the visible magnetization over a crater is found to be (non) zero, then it can be inferred that the sum $\mathcal{I}+\mathcal{E}$ is also (non) zero. Concerning the remaining toroidal part $\mathcal{T}$ of the magnetization, we note that Gubbins et al. (2011) have estimated its contribution on Earth to just 3%. Expecting its relative contribution to be similar on Mars, we consider that $\mathbf{M} \approx \mathcal{I}+\mathcal{E}$ and generalize our working hypothesis as follows: Under the assumption that the crater's magnetization did not undergo alteration since it got generated from an inducing magnetic field, its visible part is a valid proxy when it comes to the characterization of the crater as magnetized or non magnetized. Henceforth, in the following, the terms magnetization and visible magnetization are used interchangeably.

2.2. Craters Database and Relevant Metrics

Once we have calculated, thanks to equation (11), the magnetization of Mars, we concentrate on the magnetization over a number of craters. We note here, that for simplicity, throughout the paper, the word crater is employed to denote impact craters or impact basins. We choose to focus on the craters presented in Table 1 of Lillis, Robbins, et al. (2013), which have been age dated either by Frey (2008), Werner (2008), or Robbins et al. (2013). These are at the same time sufficiently large to have reset the crustal magnetization over the entire extent of the affected crust (Shahnas & Arkani-Hamed, 2007) and have clearly defined rims, so that we can safely assume they did not undergo significant resurfacing since their formation, or did so only partially (Lillis, Robbins, et al., 2013).

The features interpreted by Frey (2008, and references therein) as impact craters are quasi-circular depressions (QCDs) and crustal thin areas identified by means of Mars Orbiter Laser Altimeter (MOLA) topography data (Smith et al., 2001) and Mars Global Surveyor (MGS) radio tracking data (Neumann et al., 2004). They were dated by estimating $N(300)$, that is, the number of superimposed craters with a diameter larger than 300 km, which was then converted to an absolute age using the cratering chronology of Hartmann and Neukum (2001). Uncertainties for the determined ages were estimated by Lillis, Robbins, et al. (2013) as the square root of the number of superimposed craters on top of any particular crater, scaled to 1×10^6 km^2 and converted to absolute age using again the cratering chronology of Hartmann and Neukum (2001).

Werner (2008) mapped impact craters by means of Viking Mosaicked Digital Image Model 2 images, Mars Orbiter Camera Wide Angle image data, and MOLA topographic data. In order to infer an age estimate for craters with diameters larger than 16 km, Werner (2008) counted the superimposed craters larger than 1 km in diameter, estimated the crater size-frequency distribution (CSFD) for each crater, fitted isochrons calculated from a Martian production function (Ivanov, 2001), and applied the cratering chronology of Hartmann and Neukum (2001). Uncertainties were also given, accounting for the uncertainties of the measurements, the least squares fitting error to the isochron, and the uncertainties in the chronology model of Hartmann and Neukum (2001).

Robbins et al. (2013) mapped the rims of the craters using THermal EMission Imaging Spectrometer (THEMIS) data and MOLA topography data. Similar to Werner (2008), CSFDs were estimated for each crater, and these were used to calculate $N(D)$ crater densities. Different cutoff $N(D)$ were used for craters of different size in order to avoid saturation for older craters versus poor statistics for younger ones. Finally, two absolute isochron

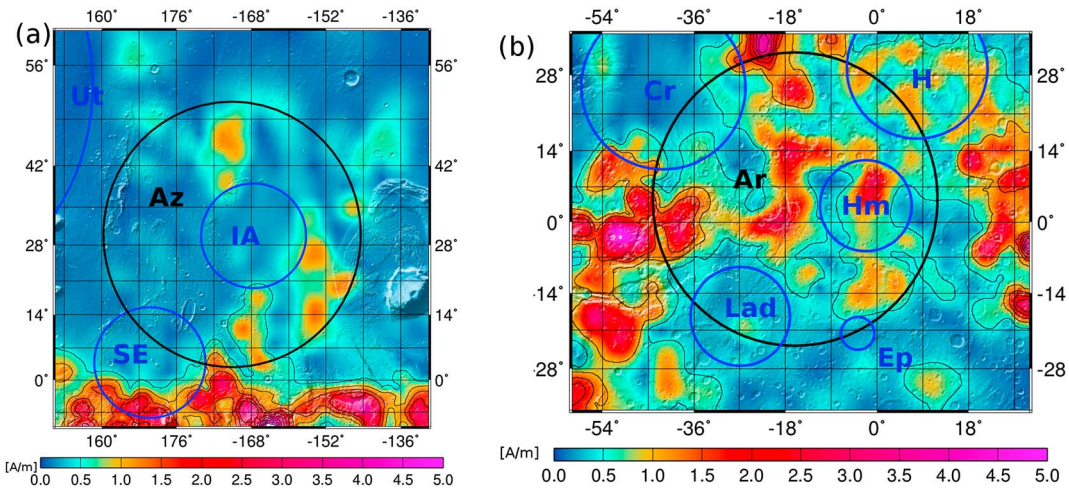

Figure 2. Extracts of the magnetization map centered on the craters (a) Amazonis and (b) Ares. The rim of the crater of interest is marked with black, whereas rims of neighboring and overlapping craters are marked with blue. The abbreviations of the craters' names are also shown; see Table 1 for the full names.

model ages were given, one based on the Neukum chronology (Ivanov, 2001; Neukum, 1983) and one on the Hartman chronology (Hartmann, 2005). Lillis, Robbins, et al. (2013) used the average of these two model ages for the craters of this database, and so do we here. Uncertainties were provided by Robbins et al. (2013), based on the square root of the number of superimposed craters.

The craters considered in our study have diameters that range between 3,380 km and 297 km. According to equation (11), the spatial resolution of our model is the same as the lithospheric field model of Morschhauser et al. (2014) and approximately equal to Backus et al. (1996, p. 103) $2\pi R_{\mathrm{Mars}} / \left(l_{\max} + \frac{1}{2}\right) = 193$ km, with $R_{\mathrm{Mars}} = 3,393.5$ km the mean reference radius of Mars and $l_{\max} = 110$ the maximum SH degree of the lithospheric field model. Consequently, the area covered by each of the considered craters falls within the resolution limits of our model.

In order to interpret a given crater as being magnetized or demagnetized, we consider jointly a number of its characteristics: the magnetization model within its vicinity, its size, the ratio between the average magnetization up to half radius distance from its center, and the average magnetization between 1 radius and 1.5 radii distance from its center, its maximum magnetization up to half radius distance from their center, and its circumferentially averaged magnetization over concentric circles of increasing radius from the crater's center (from 1% up to 150% as a function of the crater's radius, with a step size of 1%). The complete circumference of these circles is considered when there is no overlap between a given crater and another one or when the overlapping crater(s) is(are) older. This is the case for the following 24 craters: Isidis, Argyre, Hellas, Hematite, SW Daedalia, Sirenum, Amenthes, SE Elysium, North Polar, Acidalia, Solis, Prometheus, Ladon, CT3-A, CT3-C, CT3-F, Huygens, Cassini, Antoniadi, Epsilon, Tikhonravov, Eta, Iota, and Herschel. In case of overlap with features that might have affected the magnetization signature of the crater under consideration, in particular, younger craters or volcanoes, the affected part of the circles' circumference is excluded from the averaging. For this reason, the crater Amazonis has been entirely omitted from our analysis because crater In Amazonis (IA) lies at its center (see Figure 2a). For the crater Ares (see Figure 2b), the area covered by craters Hematite and Chryse is not considered because these craters are younger than Ares. The area covered by Ladon is also not considered because it is less magnetized than the bulk of Ares and the magnetization is probably related to the impact that created Ladon (see Figure 2b). A direct comparison of their age estimates is not straightforward because Ladon has been dated by Robbins et al. (2013), whereas Ares by Frey (2008), using the aforementioned, different techniques. The area covered by the younger Epsilon is not left out because it is negligibly small. For the crater CT3-D (see Figure S24 in the supporting information), the area covered by the younger craters CT3-A and Copernicus is left out. For the crater CT3-G (see Figure S25), the area covered by the crater Iota is not considered. For the crater Daedalia (see Figure S28), the area covered by the younger crater SW Daedalia is not included. Moreover, the demagnetized area in the vicinity of the volcano Arsia Mons is also left out. For the crater Zephyria (see Figure S31) the area covered by the younger craters Se Elysium,

Table 1
The Craters Considered in This Study, Along With Their Diameter, Their Absolute Model Age (See Text for Details), Their Maximum Magnetization Intensity up to Half-Radius Distance From Their Center, and the Ratio Between the Circumferential Average of the Magnetization at 1.5 and 0.1 Radii Distance From Its Center

		Model age (Ga)			$\lvert\mathcal{I}\rvert_{max}$ (A/m)	
Name	Diameter (km)	Werner (2008)	Robbins et al. (2013)	Frey (2008)	over $\pi\left(\frac{r_{crater}}{2}\right)^2$	$\mathcal{I}_{IN/OUT}$
Antoniadi (An)	400	$3.79^{+0.11}_{-0.13}$	$3.86^{+0.02}_{-0.16}$		0.49	0.45
Argyre (Ag)	1315	$3.83^{+0.11}_{-0.13}$	$3.93^{+0.05}_{-0.06}$	$4.04^{+0.04}_{-0.05}$	0.11	0.28
Herschel (Hl)	297	$3.95^{+0.11}_{-0.11}$	$3.92^{+0.06}_{-0.07}$		0.33	0.65
Isidis (Is)	1352	$3.96^{+0.1}_{-0.11}$	$3.97^{+0.04}_{-0.06}$		0.13	0.29
Huygens (Hu)	467	$3.98^{+0.1}_{-0.11}$	$4^{+0.04}_{-0.08}$		0.37	0.58
Hellas (He)	2070	$3.99^{+0.1}_{-0.11}$	$4.02^{+0.06}_{-0.15}$	$4.07^{+0.01}_{-0.04}$	0.18	0.42
Prometheus (Pro)	924		$4.04^{+0.04}_{-0.06}$		0.23	0.29
Cassini (Ca)	408	$4.03^{+0.1}_{-0.11}$	$4.06^{+0.1}_{-0.11}$		0.7	0.68
Utopia (Ut)	3380			$4.11^{+0.02}_{-0.02}$	0.16	0.46
epsilon (Ep)	358		$4.11^{+0.06}_{-0.1}$		0.26	0.69
North Polar (NP)	2145			$4.12^{+0.035}_{-0.035}$	0.18	0.59
Acidalia (Ac)	3087			$4.13^{+0.02}_{-0.02}$	0.62	0.62
SE Elysium (SE)	1403			$4.13^{+0.045}_{-0.06}$	0.79	0.37
Hematite (Hm)	1065			$4.14^{+0.05}_{-0.1}$	2.59	1.93
Chryse (Cr)	1725			$4.14^{+0.02}_{-0.02}$	0.4	0.31
Iota (Io)	325		$4.14^{+0.07}_{-0.1}$		0.99	0.36
Solis (So)	1764			$4.15^{+0.03}_{-0.05}$	0.5	0.36
CT3-F (F)	1580			$4.16^{+0.04}_{-0.05}$	0.62	0.38
Tikhonravov (Tk)	343	$4.1^{+0.1}_{-0.1}$	$4.16^{+0.07}_{-0.09}$		0.5	0.56
Ares (Ar)	3300			$4.17^{+0.01}_{-0.02}$	3.12	1.5
CT3-A (A)	1077			$4.17^{+0.045}_{-0.08}$	4.33	0.65
SW Daedalia (SW)	1278			$4.18^{+0.035}_{-0.-06}$	2.99	0.43
Ladon (Lad)	1097		$4.18^{+0.08}_{-0.08}$		0.84	0.92
CT3-D (D)	2884			$4.18^{+0.02}_{-0.03}$	20.88	2.4
CT3-G (G)	1245			$4.18^{+0.04}_{-0.06}$	7	2.9
eta (Et)	340		$4.18^{+0.08}_{-0.11}$		2.35	1.52
Sirenum (Si)	1069			$4.2^{+0.035}_{-0.065}$	4.29	0.52
Daedalia (Da)	2639			$4.2^{+0.02}_{-0.02}$	5.25	1.16
Zephyria (Ze)	1193			$4.21^{+0.04}_{-0.06}$	2.83	0.83
Amenthes (Am)	1070			$4.22^{+0.03}_{-0.05}$	0.6	0.45
CT3-C (C)	1280			$4.24^{+0.02}_{-0.05}$	3.91	0.66
CT3-H (H)	1434			$4.25^{+0.02}_{-0.04}$	1.3	1.3

Note. The last two columns are based on our model, while the rest of the information is taken from Table 1 of Lillis, Robbins, et al. (2013).

and CT3-D, and the area covered by crater deVaucouleurs is not taken into account. Finally, for the crater CT3-H the area covered by the younger craters Acidalia and Ares is left out (see Figure S30).

3. Results

Figure 1 shows our model of Mars' visible magnetization. The intensity and the three vector components, *X* (north), *Y* (east), and *Z* (down), are shown. The rims of the craters considered in our study are shown as circles on the magnetization map. The diameter of each crater is taken from Table 1 of Lillis, Robbins, et al. (2013). Table 1 lists the craters considered in this study, together with their diameter, their absolute model age, their

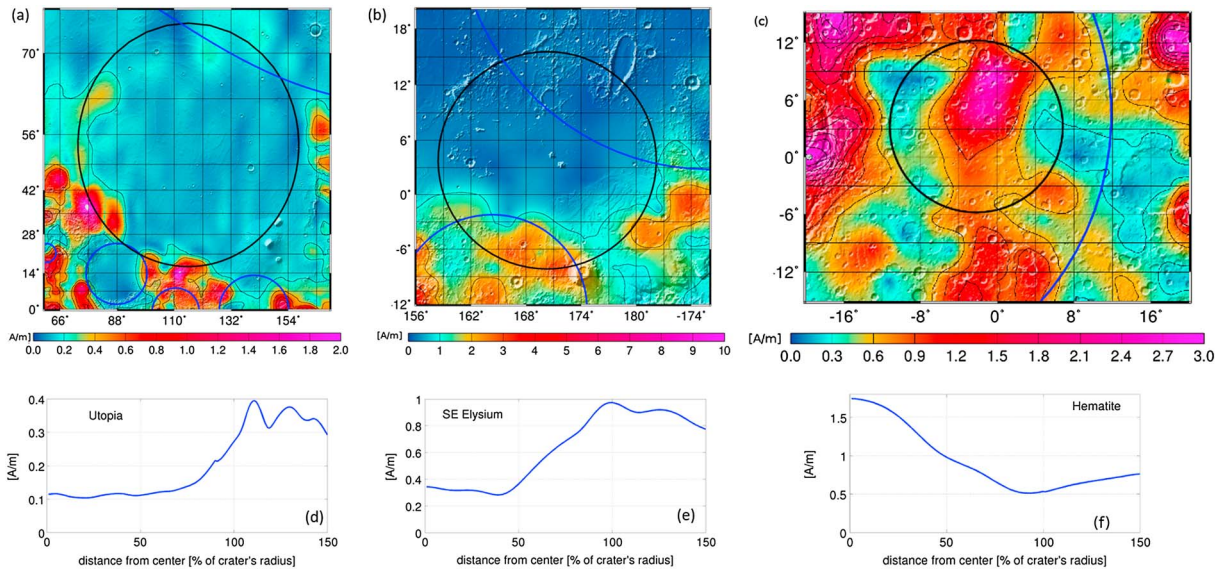

Figure 3. Extracts of the magnetization map centred on the craters (a) Utopia, (b) SE ELysium, and (c) Hematite. The rims of these craters are marked with black, whereas rims of neighboring craters are marked with blue. The circumferentially averaged magnetization over concentric circles of increasing radius from the crater's center is shown for (d) Utopia, (e) SE ELysium, and (f) Hematite.

maximum magnetization up to half radius distance from their center (denoted hereinafter as $|\mathcal{I}|_{\max,\left[0,\frac{r}{2}\right]}$), and the ratio between the average magnetization up to half radius distance from its center and the average magnetization between 1 radius and 1.5 radii distance from its center (denoted hereinafter as $\mathcal{I}_{\mathrm{IN/OUT}}$).

In order to best estimate the time of the dynamo shutoff, we ideally want to determine the youngest magnetized crater and the oldest nonmagnetized one. In Table 1, the considered craters have been ordered from the youngest to the oldest (in case of conflicting dates, craters are ordered based on the dates given by Werner, 2008). Keeping in mind that demagnetization and remagnetization processes can in some cases affect only the central part of the crater, we base our suggestion for the dynamo shutoff date on craters that are larger than twice our resolution limit, that is, the craters with at least 400 km diameter (Cassini, with a diameter of 408 km, is also excluded). North Polar is the oldest crater whose magnetization within half radius distance from its center does not exceed the noise threshold of our map. This is estimated to be around 0.2 A/m, which is roughly the maximum magnetization over the Tharsis region. However, since North Polar is located in a region of low magnetization (see Figure S11), we choose the slightly older crater Utopia as our reference crater for the dynamo shutoff. The magnetization of Utopia within half-radius distance is also below the threshold noise, while at the same time is clearly less magnetized than its surroundings, with a ratio $\mathcal{I}_{\mathrm{IN/OUT}} = 0.46$. Concerning the determination of the younger magnetized crater, we observe that craters Acidalia and SE Elysium carry non negligible magnetization close to their center, with $|\mathcal{I}|_{\max,\left[0,\frac{r}{2}\right]}$ equal to 0.62 and 0.79 A/m, respectively. Even though these craters are less magnetized than their surroundings, with $\mathcal{I}_{\mathrm{IN/OUT}}$ equal to 0.62 and 0.37, respectively, the only way to account for the magnetization close to their centers is to consider that the dynamo was still active when these craters formed. The youngest strongly magnetized crater, according to the dating suggested by Frey (2008), is Hematite with $|\mathcal{I}|_{\max,\left[0,\frac{r}{2}\right]} = 2.59$. The magnetization maps of Utopia, SE Elysium, and Hematite, together with their circumferentially averaged magnetization profiles, are shown in Figure 3. We infer that the dynamo shut off before the crust within Utopia cooled below its magnetic blocking temperature and much probably after the formation of SE Elysium and Acidalia but certainly after the formation of Hematite.

In order to go a step further and infer from our results a specific time interval for the dynamo shutdown, we need to account also for the age uncertainties that characterize the dating of the craters. To do so, we opt for the probabilistic approach of Lillis et al. (2008), which accounts jointly for the age uncertainties of many craters. The assumption of this approach is that the number of superimposed craters, $N(\mathrm{D})$, for a given crater follows a Poisson distribution. By dividing a set of craters into magnetized and nonmagnetized, one can assign a probability to a given date and duration of dynamo shutoff by multiplying the probabilities that all demagnetized craters are younger than the end of the dynamo cessation and all magnetized craters are older

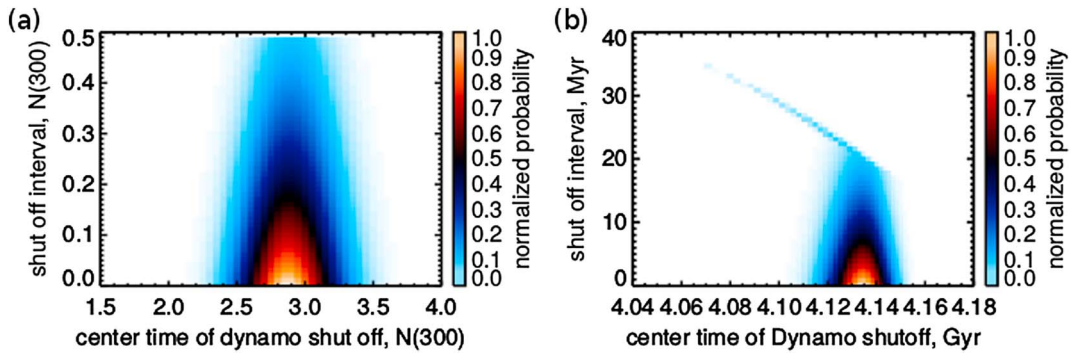

Figure 4. Normalized probabilities as a function of the time at which the dynamo ceased operating, in terms of (a) *N*(300) crater retention age and (b) absolute model age using the cratering chronology of Hartmann and Neukum (2001).

than the beginning of the cessation. For this calculation we focus only on the craters dated by Frey (2008) because the database by Robbins et al. (2013) includes only one sufficiently large crater we found to be magnetized, crater Ladon, while the database by Werner (2008) includes only craters found to be demagnetized. We perform this calculation for time intervals over which the dynamo ceased rather than specific dates (see Figure 2b by Lillis et al., 2008, for an illustration of the concept). The results, shown in Figure 4, suggest that the dynamo shut down between *N*(300) = 2.5 – 3.2, where the uncertainty corresponds to the 1 σ area in Figure 4a, or between 4.12 and 4.14 Ga when *N*(300) is converted to an absolute age by using the cratering chronology of Hartmann and Neukum (2001).

Looking now at the magnetization signatures of the oldest craters, we observe that crater Amenthes (see Figure 5) has both relatively low magnetization close to its center, with $|\mathcal{I}|_{\max,\left[0,\frac{r}{2}\right]} = 0.6$ A/m, and is much less magnetized than its surroundings, with $\mathcal{I}_{\mathrm{IN/OUT}} = 0.45$. If its magnetization pattern is not due to postimpact modifications, it might indicate that the dynamo has been weaker when Amenthes acquired its magnetization than at earlier or later stages. This, in turn, hints to the possibility of a dynamo magnetic field that has not been constant throughout its history. The iron snow regime has been shown to be a driving mechanism that can account for a weak magnetic field (see, e.g., Vilim et al., 2010, for a study on Mercury and Breuer et al., 2015, for a review on possible dynamo driving mechanisms for planetary bodies). In any case we note that since its visible magnetization is nonzero, its null space is also nonzero. It could be that an important part of its magnetization is part of its current null space.

In the supporting information, we present extracts of the visible magnetization intensity map over all craters considered in this study (see Figures S1 – S32). The rim of the crater under consideration is marked with black, and the rims of neighboring craters are marked with blue.

4. Discussion

Our results are in close agreement with previous studies based on impact craters that have suggested the dynamo shut down around 4.1 Ga ago (e.g., Arkani-Hamed, 2004; Lillis, Robbins, et al., 2013). It is also in close

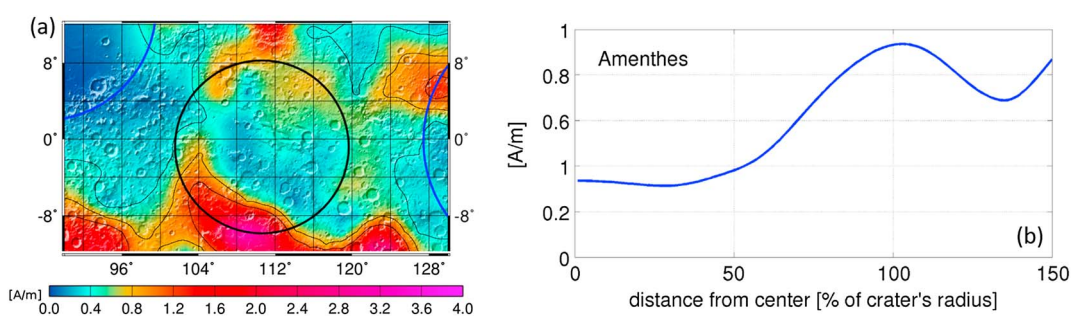

Figure 5. (a) Extract of the magnetization map centered on the crater Amenthes. Its rim is marked with black, whereas rims of neighboring craters are marked with blue. (b) The circumferentially averaged magnetization over concentric circles of increasing radius from the crater's center.

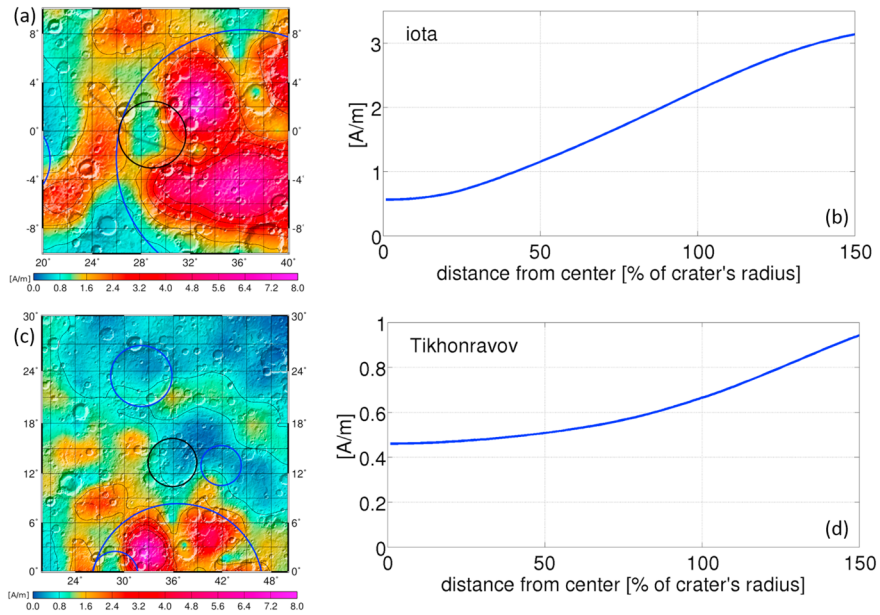

Figure 6. Extracts of the magnetization map centered on the craters (a) Iota and (c) Tikhonravov. The rims of these craters are marked with black, whereas rims of neighboring craters are marked with blue. The circumferentially averaged magnetization over concentric circles of increasing radius from the crater's center is shown for (b) Iota and (d) Tikhonravov.

agreement with the study based on the Allan Hills meteorite ALH84001 that concluded that one component of its magnetization is 4.1 Ga old, while another is 3.9–4.1 Ga old (see, e.g., Antretter et al., 2003; Shuster & Weiss, 2005; Weiss, Shuster et al., 2002; Weiss, Vali et al., 2002). We note that this result indicates that the dynamo was active prior to, and possibly as late as, 3.9–4.1 Ga ago because the sample may have been magnetized in a crustal magnetic field.

Evidently, any inferences for the history of the dynamo depend strongly on the accuracy of the age estimates for the studied craters. In this respect, it is worth underlining that the dating of craters is far from a standardized technique and is based on a large number of assumptions (for more details on this subject see, e.g., Robbins et al., 2013, and Werner, 2014, and references therein). Looking at Table 1, we observe discrepancies among craters dated by different methods. We observe, moreover, that the dates given by Frey (2008) are consistently older than the dates given by Werner (2008) and/or Robbins et al. (2013). More recently, Werner (2014) reported that absolute model ages derived by Frey (2008) for some QCDs could be significantly overestimated. Moreover, according to Werner et al. (2014), the absolute age of Martian craters should be in general shifted by 100–200 Ma backward. Naturally, any revision of these dates and their uncertainties would lead to a revision of our suggested interval for the dynamo shutoff date.

Further insight into the history of the Martian magnetic field could be obtained by studying the magnetization signature of smaller craters. Looking at Table 1, we see that craters Antoniadi, Herschel, Huygens, and Cassini have magnetizations within half-radius distance from their center larger than the estimated noise threshold of our map. However, it is difficult to determine whether they are magnetized or demagnetized because their radius is at the limit of the spatial resolution of our model, that is why we did not take into account these craters in our search for the youngest magnetized crater. As far as the search for the oldest magnetized crater is concerned, we note that key craters are Iota and Tikhonravov. Iota, with a diameter of 325 km, carries non-negligible magnetization close to its center with $|\mathcal{I}|_{\max,\left[0,\frac{r}{2}\right]}=0.99$ A/m (see also Figures 6a and 6b) but at the same time is much less magnetized than its surroundings, with $\mathcal{I}_{\mathrm{IN/OUT}}=0.36$. Because of the finite spatial resolution of our model, there is a limit to the magnetization gradients that it can reproduce (see, e.g., Langlais and Thébault, 2011, Lillis et al., 2010, and Lillis, Robbins, et al., 2013, for relevant discussions). Defining this limit is not straightforward and is beyond the scope of this study. We note, however, that in the case

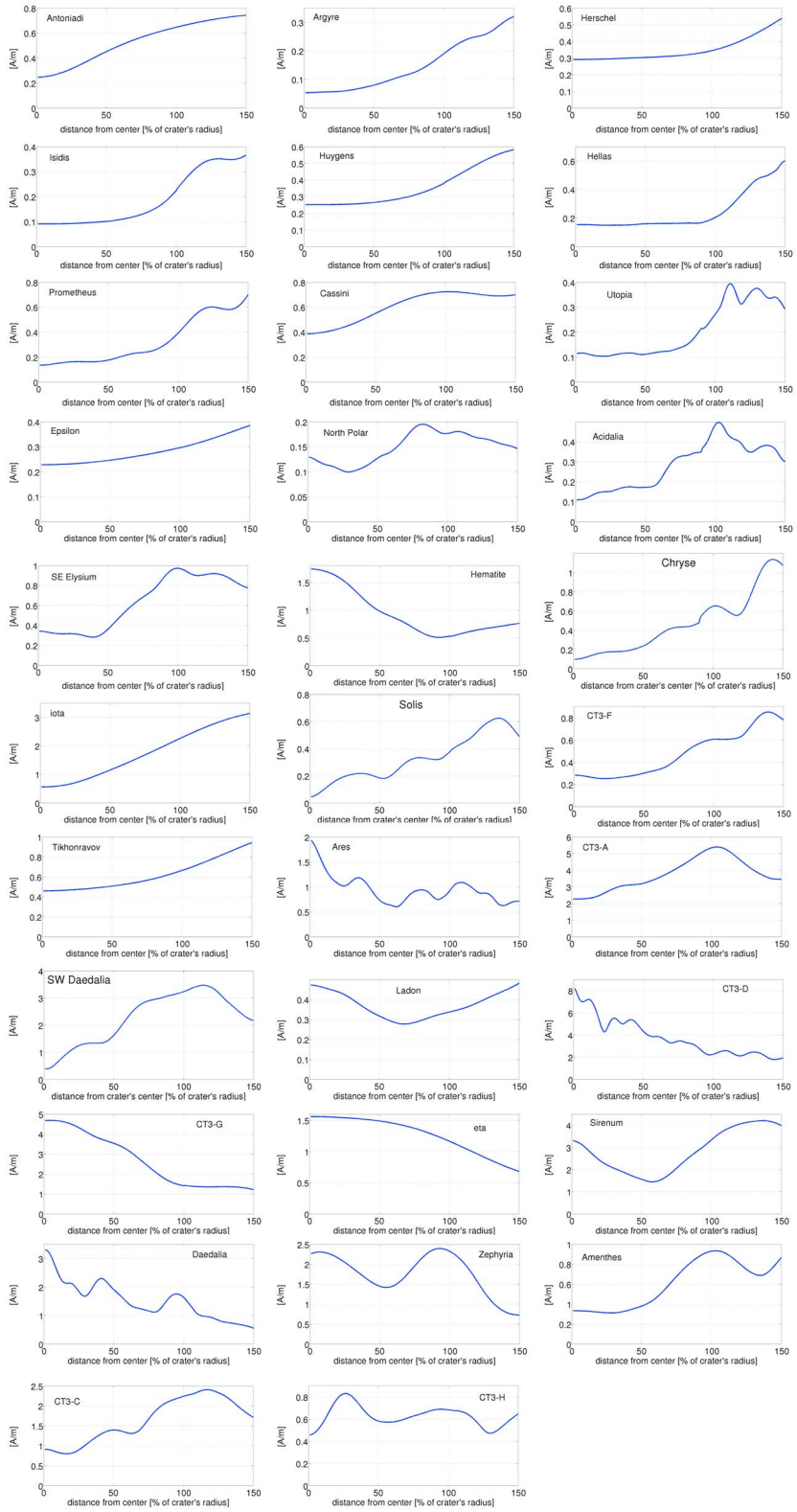

Figure 7. The circumferentially averaged magnetization intensity profiles of all craters considered in this study, as a function of the distance from the crater's center. The magnetization profiles are ordered chronologically, from the youngest (top left corner) to the oldest (bottom right corner), according to each crater's best age estimate, independently of the database to which they belong. In case of conflicting dates, craters are ordered based on the dates given by Werner (2008).

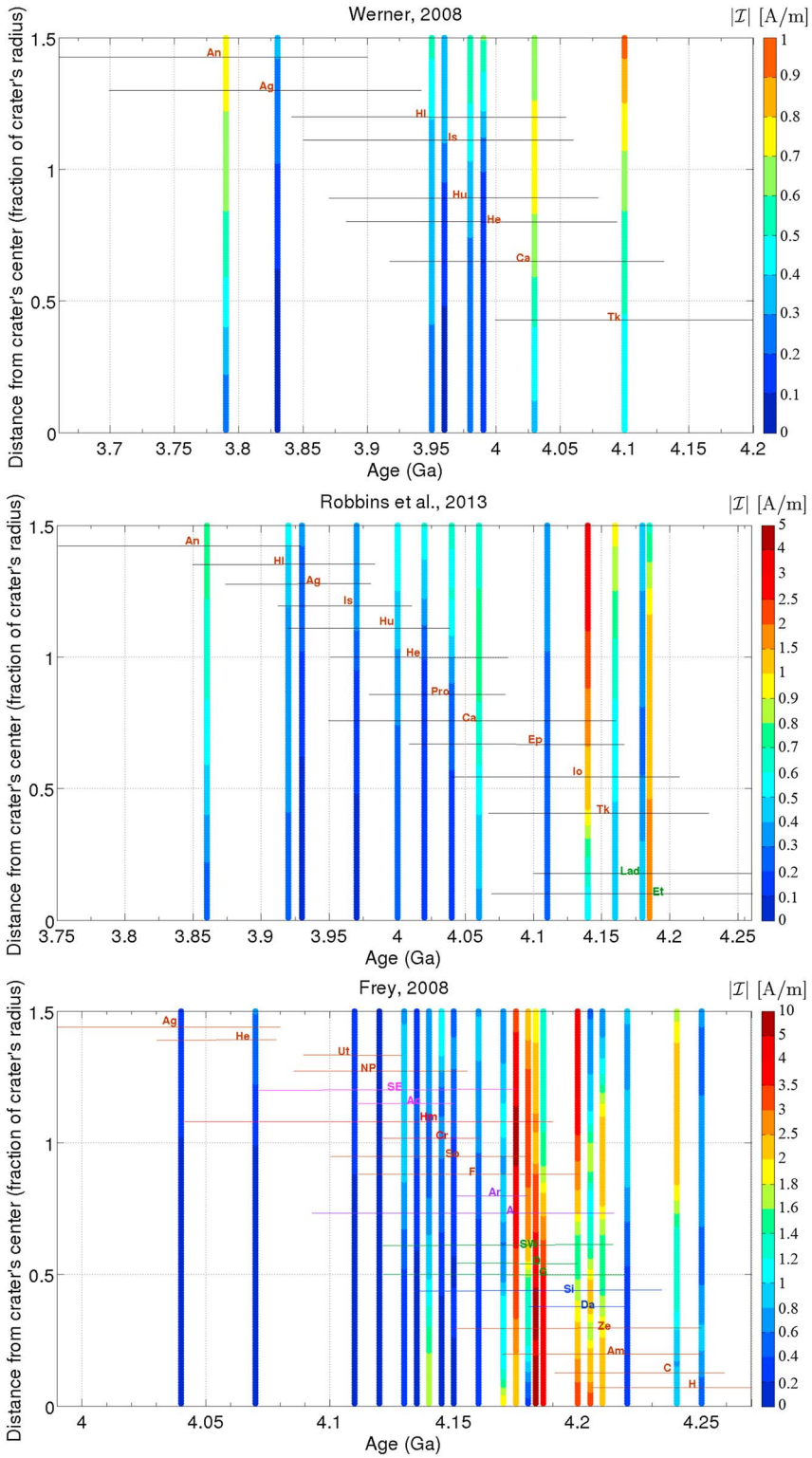

Figure 8. The circumferentially averaged magnetization intensity profiles of all craters considered in this study, as a function of the distance from the crater's center. The magnetization profiles are ordered in time, according to each crater's best age estimate. From top to bottom: the magnetization profiles of craters whose ages are given by Werner (2008), Robbins et al. (2013), and Frey (2008). Age uncertainties are also shown as horizontal bars (based on Werner, 2008, Robbins et al., 2013, and Lillis, Robbins, et al., 2013). Craters with the same best age estimate have their abbreviated name and age uncertainty bar marked with the same color, other than brown. See Table 1 for the full names of the craters.

of Iota, it could be that its magnetization values are actually lower than our model can predict, given its size and the magnetization intensity of its surroundings. Were Iota a demagnetized crater, the implications for the dynamo shutoff date are not clear since Iota is dated by Robbins et al. (2013) while Acidalia, SE ELysium, and Hematite are dated by Frey (2008). Tikhonravov is only slightly larger than Iota, with a diameter of 343 km. With $|\mathcal{I}|_{\max,\left[0,\frac{r}{2}\right]} = 0.5$ A/m (see also Figures 6c and 6d) and $\mathcal{I}_{\mathrm{IN/OUT}} = 0.56$ it could also qualify as a crater that could perhaps be demagnetized. If it were demagnetized, the implications for the dynamo shutoff date are again unclear because the estimated ages given by Werner (2008) and Robbins et al. (2013) do not agree with each other. Moreover, taken together, they cover the entire period of interest from 4 Ga up to 4.23 Ga.

The circumferentially averaged magnetization profiles of all craters, ordered in the same way as in Table 1, are shown in Figure 7. Looking at this figure, we observe that craters up to Tikhonravov, with the exception of the nonmagnetized North Polar and the magnetized Hematite, are less magnetized close to their center than close to their rims (note that the magnetization profiles extend beyond the crater's rim, up to a distance of 150% of the crater's radius from the crater's center). This becomes also apparent by looking at Figure 8, which shows the circumferentially averaged magnetization profiles of all craters separately for each age database, together with the age uncertainties. The color scale for each database has been selected so that it facilitates the observation of the magnetization spatial gradients. As already mentioned, the (de)magnetization procedure can vary from case to case, depending on the characteristics of the impact and the affected crust. Moreover, postimpact alterations, such as sedimentation, vary regionally. Therefore, we point out this pattern of almost monotonically increasing magnetization profiles up to the time that Tikhonravov was created (with the exception of Hematite and the completely non magnetized North Polar), but we do not infer from this conclusions concerning the classification of these craters as magnetized or demagnetized.

As a last point, we note that our magnetization map cannot be used to infer paleopole positions without additional assumptions or prior information. According to Vervelidou et al. (2017), in order for paleopole positions to be accurately estimated, the direction of the entire magnetization should be reconstructed, and not only the direction of its visible part.

5. Conclusions

In this study, we derived a mathematical formula that allows the conversion of any set of SH lithospheric magnetic field coefficients to a set of vector SH coefficients of the visible part of the magnetization (see equation (11). By visible part we mean the part of the magnetization that has given rise to the observed magnetic field of lithospheric origin (see Vervelidou et al., 2017). The assumption that underlines this conversion formula is that the magnetized layer is a spherical shell of constant thickness, where the magnetization varies only laterally.

Based on this formula, we convert the lithospheric magnetic field model of Mars provided by Morschhauser et al. (2014) into a visible magnetization model with a spatial resolution of approximately 200 km (see Figure 1). Further on, we provide analytical formulas for the vector SH coefficients of the visible magnetization of induced origin and for the vector SH coefficients of the respective null space, as functions of the SH coefficients of the susceptibility and of the inducing field. Based on these formulas, we show that for craters that have not undergone major alterations since their (de)magnetization, their entire magnetization is zero if and only if their visible magnetization is zero (see equations (B8) and (B9).

According to the magnetization signatures of the craters considered here, we infer that the dynamo shut off after the impacts that created Acidalia and SE Elysium and before the crust within Utopia cooled below its magnetic blocking temperature. Further on, by following the probabilistic approach of Lillis et al. (2008), which accounts jointly for the uncertainties of the craters estimated age, we infer that the dynamo shutoff occurred at an absolute model age of 4.12–4.14 Ga.

Due to the spatial resolution of our model and the complexities in the (de)magnetization process, we base our conclusions only on craters whose diameter is at least 400 km. Magnetic field data of higher resolution, delivered by the Mars Atmosphere and Volatile EvolutioN mission (see, e.g., Connerney et al., 2015), will allow the estimation of the visible magnetization up to a higher SH degree. Consequently, the magnetization signatures of small craters, like Iota and Tikhonravov, in combination with more precise dating, can narrow done this interval.

Finally, our study offers some hints that the driving mechanism of the Martian dynamo was not the same throughout its history. The weak magnetization observed over Amenthes, one of the oldest Martian craters, could indicate that the dynamo was weaker at that stage than at earlier or later stages. A possible mechanism that could account for such a behavior could be the iron snow regime, which has been argued by Stewart et al. (2007) to be a mechanism that could reestablish the Martian dynamo in the future.

Appendix A: Converting a SH Lithospheric Magnetic Field Model Into a Visible Magnetization Model

In this section, we derive a formula that converts any set of magnetic field SH coefficients to a set of visible magnetization SH coefficients, under the assumption that the magnetization is confined to a spherical layer of finite thickness and varies only laterally. This derivation follows closely the derivation presented by Vervelidou et al. (2017) for a similar conversion formula under the assumption that the magnetized layer is infinitesimally thin (for a different derivation of this latter formula see Gubbins et al., 2011).

We consider the magnetized spherical layer to have thickness t and to be the upper layer of a sphere with radius R, where R is the reference radius of the magnetic field SH coefficients.

Under the aforementioned assumptions, the layer's entire magnetization distribution, $\mathbf{M}$, reads

$$\begin{aligned}\mathbf{M}(\mathbf{r}') &= \mathbf{M}(r', \theta', \phi') \\ &= \mathbf{f}(r')\mathbf{g}(\theta', \phi') \\ &= \mathbf{g}(\theta', \phi'),\end{aligned} \tag{A1}$$

where $\mathbf{f}(r')$ represents the radially varying part of $\mathbf{M}$, assumed to be equal to 1, and $\mathbf{g}(\theta', \phi')$ represents the laterally varying part.

We have (e.g., Blakely, 1996, equation (5.2))

$$V(\mathbf{r}) = \frac{\mu_0}{4\pi} \int_{\Omega'} \mathbf{M}(\mathbf{r}')\nabla' \left(\frac{1}{|\mathbf{r} - \mathbf{r}'|} \right) \mathrm{d}\Omega', \tag{A2}$$

with V the magnetic potential at point $\mathbf{r}$ due to the magnetization distribution $\mathbf{M}$ that lies in the magnetized volume Ω'.

Introducing equation (A1) into equation (A2), we obtain

$$V(\mathbf{r}) = \frac{\mu_0}{4\pi} \int_{\Omega} \mathbf{g}(\theta', \phi')\nabla' \left(\frac{1}{|\mathbf{r} - \mathbf{r}'|} \right) \mathrm{d}\Omega', \tag{A3}$$

with $\mathrm{d}\Omega' = (r')^2 \sin\theta' \mathrm{d}\theta' \mathrm{d}\phi' \mathrm{d}r'$.

According to equation (1), $\mathbf{g}$ can be split into its $\mathcal{I}$, $\mathcal{E}$, and $\mathcal{T}$ parts. This gives

$$\begin{aligned}V(\mathbf{r}) = &\frac{\mu_0}{4\pi} \int_{\Omega} \mathcal{I}(\theta', \phi')\nabla' \left(\frac{1}{|\mathbf{r} - \mathbf{r}'|} \right) \mathrm{d}\Omega' \\ &+ \frac{\mu_0}{4\pi} \int_{\Omega} \mathcal{E}(\theta', \phi')\nabla' \left(\frac{1}{|\mathbf{r} - \mathbf{r}'|} \right) \mathrm{d}\Omega' \\ &+ \frac{\mu_0}{4\pi} \int_{\Omega} \mathcal{T}(\theta', \phi')\nabla' \left(\frac{1}{|\mathbf{r} - \mathbf{r}'|} \right) \mathrm{d}\Omega'.\end{aligned}$$

By expressing $\mathcal{I}$, $\mathcal{E}$, and $\mathcal{T}$ in vector SH according to equations (2)–(4) and replacing the term $\nabla' \left(\frac{1}{|\mathbf{r}-\mathbf{r}'|} \right)\Big|_{r'=r''}$ by its SH expansion, it turns out that the contribution of $\mathcal{E}$ and $\mathcal{T}$ to V is zero, and equation (A3) writes

$$
\begin{aligned}
V(\mathbf{r}) &= \frac{\mu_0}{4\pi}\int_{\Omega}\mathcal{I}(\theta',\phi')\nabla'\left(\frac{1}{|\mathbf{r}-\mathbf{r}'|}\right)\mathrm{d}\Omega' \\
&= \frac{\mu_0}{4\pi}\int_{R-t}^{R}\int_0^{\pi}\int_0^{2\pi}\sum_{l'}\sum_{m'}\left[g^{m'}_{\mathcal{I},l'}Y^{m',c}_{l'}(\theta',\phi')+h^{m'}_{\mathcal{I},l'}Y^{m',s}_{l'}(\theta',\phi')\right]\left(\sqrt{\frac{l'}{2l'+1}}\right)\cdot \\
&\frac{1}{r^2}\sum_{l}\sum_{m}l\left(\frac{r''}{r}\right)^{l-1}\left[Y^{m,c}_{l}(\theta,\phi)Y^{m,c}_{l}(\theta',\phi')+Y^{m,s}_{l}(\theta,\phi)Y^{m,s}_{l}(\theta',\phi')\right]\mathrm{d}\Omega' \\
&+\frac{\mu_0}{4\pi}\int_{R-t}^{R}\int_0^{\pi}\int_0^{2\pi}\sum_{l'}\sum_{m'}\left[g^{m'}_{\mathcal{I},l'}\frac{\partial Y^{m',c}_{l'}(\theta',\phi')}{\partial\theta'}+h^{m'}_{\mathcal{I},l'}\frac{\partial Y^{m',s}_{l'}(\theta',\phi')}{\partial\theta'}\right]\left(\sqrt{\frac{1}{l'(2l'+1)}}\right)\cdot \\
&\frac{1}{rr''}\sum_{l}\sum_{m}\left(\frac{r''}{r}\right)^{l}\left[Y^{m,c}_{l}(\theta,\phi)\frac{\partial Y^{m,c}_{l}(\theta',\phi')}{\partial\theta'}+Y^{m,s}_{l}(\theta,\phi)\frac{\partial Y^{m,s}_{l}(\theta',\phi')}{\partial\theta'}\right]\mathrm{d}\Omega' \\
&+\frac{\mu_0}{4\pi}\int_{R-t}^{R}\int_0^{\pi}\int_0^{2\pi}\sum_{l'}\sum_{m'}\left[g^{m'}_{\mathcal{I},l'}\frac{\partial Y^{m',c}_{l'}(\theta',\phi')}{\partial\phi'}+h^{m'}_{\mathcal{I},l'}\frac{\partial Y^{m',s}_{l'}(\theta',\phi')}{\partial\phi'}\right]\left(\sqrt{\frac{1}{l'(2l'+1)}}\right)\frac{1}{\sin\theta'}\cdot \\
&\frac{1}{rr''\sin\theta'}\sum_{l}\sum_{m}\left(\frac{r''}{r}\right)^{l}\left[Y^{m,c}_{l}(\theta,\phi)\frac{\partial Y^{m,c}_{l}(\theta',\phi')}{\partial\phi'}+Y^{m,s}_{l}(\theta,\phi)\frac{\partial Y^{m,s}_{l}(\theta',\phi')}{\partial\phi'}\right]\mathrm{d}\Omega'.
\end{aligned}
$$

Integrating now over r', θ', and ϕ', while accounting for well known properties of the spherical harmonics, we obtain

$$
V(\mathbf{r}) = \mu_0\sum_{l}\sum_{m}\left(\sqrt{\frac{l}{2l+1}}\right)\left(\frac{R}{l+2}\right)\left(\frac{R}{r}\right)^{l+1}\left[1-\left(1-\frac{t}{R}\right)^{l+2}\right]\left(g^{m}_{\mathcal{I},l}Y^{m,c}_{l}+h^{m}_{\mathcal{I},l}Y^{m,s}_{l}\right). \tag{A4}
$$

The magnetic potential $V(\mathbf{r})$ can also be expanded in spherical harmonics:

$$
V(\mathbf{r}) = R\sum_{l}\sum_{m}\left(\frac{R}{r}\right)^{l+1}\left(g^{m}_{l}Y^{m,c}_{l}+h^{m}_{l}Y^{m,s}_{l}\right). \tag{A5}
$$

Equating the right-hand side of equations (A4) and (A5), multiplying both sides of the new equation with the real spherical harmonics, integrating over the surface of a sphere, and accounting for the orthogonality properties of the SH functions, we obtain the following relationship between the coefficients $\left\{g^{m}_{l},h^{m}_{l}\right\}$ of V and the coefficients $\left\{g^{m}_{\mathcal{I},l},h^{m}_{\mathcal{I},l}\right\}$ of $\mathcal{I}$:

$$
\left\{\begin{matrix} g^{m}_{\mathcal{I},l} \\ h^{m}_{\mathcal{I},l}\end{matrix}\right\} = \frac{l+2}{\mu_0}\sqrt{\frac{2l+1}{l}}\frac{1}{\left[1-\left(1-\frac{t}{R}\right)^{l+2}\right]}\left\{\begin{matrix} g^{m}_{l} \\ h^{m}_{l}\end{matrix}\right\}, \tag{A6}
$$

where $\left\{g^{m}_{l},h^{m}_{l}\right\}$ are given in nanotesla and $\left\{g^{m}_{\mathcal{I},l},h^{m}_{\mathcal{I},l}\right\}$ in units of nA/m.

Appendix B: Relationship Between $\mathcal{I}$ and $\mathcal{E}$ in Case of Induced Magnetization

A magnetization distribution of induced geometry, $\mathbf{M}_{\text{induced}}$, can be written as (see, e.g, equations (1.15)–(1.17) of Langel & Hinze, 1998)

$$
\mathbf{M}_{\text{induced}}(\mathbf{r}) = \frac{\chi(\mathbf{r})}{\mu_0}\mathbf{B}_{\text{inducing}}(\mathbf{r}), \tag{B1}
$$

with $\mathbf{r}$ the position vector of the magnetized point, $\mathbf{B}_{\text{inducing}}$ the inducing magnetic field, $\chi(\mathbf{r})$ the susceptibility at point $\mathbf{r}$, and μ_0 the magnetic permeability of empty space. The contribution of the induced magnetic field is not taken into account in the above equation because it is negligibly small when compared to that of the inducing magnetic field. Expressing now both the susceptibility distribution and the inducing magnetic field in terms of SH, we obtain

$$
\mathbf{M}_{\text{induced}} = \sum_{\tilde{l}}\sum_{\tilde{m}=-\tilde{l}}^{\tilde{l}}\alpha^{\tilde{m}}_{\tilde{l}}Y^{\tilde{m}}_{\tilde{l}}\frac{1}{\mu_0}\left\{-\nabla\left[R\sum_{l'}\sum_{m'=-l'}^{l'}g^{m'}_{l'}Y^{m'}_{l'}\left(\frac{R}{r}\right)^{l+1}\right]\right\}, \tag{B2}
$$

with $\alpha_{\tilde{l}}^{\tilde{m}}$ the Gauss coefficients of the susceptibility distribution, $g_{l'}^{m'}$ the Gauss coefficients of the inducing magnetic field, and

$$Y_l^m = \begin{cases} Y_l^{m,c} = P_l^m(\cos\theta)\cos(m\phi), & m \geq 0 \\ Y_l^{m,s} = P_l^m(\cos\theta)\sin(m\phi), & m < 0 \end{cases} \tag{B3}$$

the Schmidt seminormalized real spherical harmonics of degree l and order m.

Considering now that the $\mathcal{T}$ part of $\mathbf{M}_{\text{induced}}$ is negligibly small (see Gubbins et al., 2011, for an estimation of its contribution in the Earth's induced magnetization), $\mathbf{M}_{\text{induced}}$ according to equation (1) reads

$$\mathbf{M}_{\text{induced}} = \mathcal{I} + \mathcal{E} \tag{B4}$$

$$= \sum_l \sum_{m=0}^{l} g_{\mathcal{I},l}^m \mathbf{Y}_{l,l-1}^{m,c} + h_{\mathcal{I},l}^m \mathbf{Y}_{l,l-1}^{m,s} + \sum_l \sum_{m=0}^{l} g_{\mathcal{E},l}^m \mathbf{Y}_{l,l+1}^{m,c} + h_{\mathcal{E},l}^m \mathbf{Y}_{l,l+1}^{m,s}. \tag{B5}$$

Thanks to the orthogonality of vector SH, we obtain

$$\begin{Bmatrix} g_{\mathcal{I},l}^m \\ h_{\mathcal{I},l}^m \end{Bmatrix} = \frac{2l+1}{4\pi} \int \mathbf{M}_{\text{induced}} \cdot \begin{Bmatrix} \mathbf{Y}_{l,l-1}^{m,c} \\ \mathbf{Y}_{l,l-1}^{m,s} \end{Bmatrix} \mathrm{d}\Omega \tag{B6}$$

and

$$\begin{Bmatrix} g_{\mathcal{E},l}^m \\ h_{\mathcal{E},l}^m \end{Bmatrix} = \frac{2l+1}{4\pi} \int \mathbf{M}_{\text{induced}} \cdot \begin{Bmatrix} \mathbf{Y}_{l,l+1}^{m,c} \\ \mathbf{Y}_{l,l+1}^{m,s} \end{Bmatrix} \mathrm{d}\Omega \tag{B7}$$

Introducing now equation (B2) into equations B6 and B7, we obtain

$$\begin{Bmatrix} g_{\mathcal{I},l}^m \\ g_{\mathcal{E},l}^m \end{Bmatrix} = \frac{2l+1}{4\pi\mu_0} \sum_{\tilde{l},l'} \left(\frac{R}{r}\right)^{l'+2} \begin{Bmatrix} A_{l,l',\tilde{l}} \\ B_{l,l',\tilde{l}} \end{Bmatrix} \sum_{\tilde{m}=-\tilde{l}}^{\tilde{l}} \sum_{m'=-l'}^{l'} \alpha_{\tilde{l}}^{\tilde{m}} g_{l'}^{m'} \int Y_{\tilde{l}}^{\tilde{m}} Y_{l'}^{m'} Y_l^{m,c} \mathrm{d}\Omega, \tag{B8}$$

and

$$\begin{Bmatrix} h_{\mathcal{I},l}^m \\ h_{\mathcal{E},l}^m \end{Bmatrix} = \frac{2l+1}{4\pi\mu_0} \sum_{\tilde{l},l'} \left(\frac{R}{r}\right)^{l'+2} \begin{Bmatrix} A_{l,l',\tilde{l}} \\ B_{l,l',\tilde{l}} \end{Bmatrix} \sum_{\tilde{m}=-\tilde{l}}^{\tilde{l}} \sum_{m'=-l'}^{l'} \alpha_{\tilde{l}}^{\tilde{m}} g_{l'}^{m'} \int Y_{\tilde{l}}^{\tilde{m}} Y_{l'}^{m'} Y_l^{m,s} \mathrm{d}\Omega, \tag{B9}$$

where

$$A_{ll'\tilde{l}} = (l'+1)\sqrt{\frac{l}{2l+1}} - \frac{C_{ll'\tilde{l}}}{\sqrt{l(2l+1)}} \tag{B10}$$

and

$$B_{ll'\tilde{l}} = \frac{C_{ll'\tilde{l}}}{(l+1)(2l+1)} - (l'+1)\sqrt{\frac{(l+1)}{2l+1}}, \tag{B11}$$

with

$$C_{ll'\tilde{l}} = \frac{l'(l'+1) + l(l+1) - \tilde{l}(\tilde{l}+1)}{2}. \tag{B12}$$

According to equation (B8), if $g_{\mathcal{I},l}^m \neq 0$ then $g_{\mathcal{E},l}^m \neq 0$ and vice versa, and according to equation (B9), if $h_{\mathcal{I},l}^m \neq 0$, then $h_{\mathcal{E},l}^m \neq 0$ and vice versa. We conclude that a magnetization of induced geometry is (non) zero if and only if its visible magnetization is also (non) zero.

Acknowledgments
The authors wish to thank an anonymous reviewer for valuable comments and Stephanie Werner for useful discussions concerning the dating of the craters. This work was funded by the Deutsche Forschungsgemeinschaft (DFG, German Research Foundation), within the Schwerpunktprojekt 1488-Planetary Magnetism under grants LE2477/3-2 (F. V. and V. L.) and GR3751/1-1 (A. M. and M. G.). It is based on the lithospheric magnetic field model of Mars by Morschhauser et al. (2014), whose spherical harmonic coefficients are available online as supporting information of the respective article. This is IPGP publication 3896.

References

Acuña, M. H., Connerney, J. E. P., Lin, R. P., Mitchell, D., Carlson, C. W., McFadden, J., & Wasilewski, P. (1999). Global distribution of crustal magnetization discovered by the Mars Global Surveyor MAG/ER experiment. *Science*, *284*(5415), 790–793.

Acuña, M. H., Connerney, J. E. P., Wasilewski, P., Lin, R. P., Mitchell, D., Anderson, K. A., & Vignes, D. (2001). Magnetic field of Mars: Summary of results from the aerobraking and mapping orbits. *Journal of Geophysical Research*, *106*(E10), 23,403–23,417.

Antretter, M., Fuller, M., Scott, E., Jackson, M., Moskowitz, B., & Solheid, P. (2003). Paleomagnetic record of Martian meteorite ALH84001. *Journal of Geophysical Research*, *108*(E6), 5049. https://doi.org/10.1029/2002JE001979

Arkani-Hamed, J. (2002). Magnetization of the Martian crust. *Journal of Geophysical Research*, *107*(E5), 5032. https://doi.org/10.1029/2001JE001496

Arkani-Hamed, J. (2004). Timing of the Martian core dynamo. *Journal of Geophysical Research*, *109*, E03006. https://doi.org/10.1029/2003JE002195

Arkani-Hamed, J. (2005). Magnetic crust of Mars. *Journal of Geophysical Research*, *110*, E08005. https://doi.org/10.1029/2004JE002397

Backus, G., Parker, R., & Constable, C. (1996). *Foundations of geomagnetism*. Cambridge, UK: Cambridge University Press.

Blakely, R. J. (1996). *Potential theory in gravity and magnetic applications*. Cambridge, UK: Cambridge University Press.

Breuer, D., Labrosse, S., & Spohn, T. (2010). Thermal evolution and magnetic field generation in terrestrial planets and satellites. *Space Science Reviews*, *152*, 449–500.

Breuer, D., Rueckriemen, T., & Spohn, T. (2015). Iron snow, crystal floats, and inner-core growth: Modes of core solidification and implications for dynamos in terrestrial planets and moons. *Progress in Earth and Planetary Science*, *2*(1), 39.

Connerney, J. E. P., Acuna, M. H., Ness, N. F., Spohn, T., & Schubert, G. (2004). Mars crustal magnetism. *Space Science Reviews*, *111*(1-2), 1–32.

Connerney, J. E. P., Acuna, M. H., Wasilewski, P. J., Kletetschka, G., Ness, N. F., Reme, H., & Mitchell, D. L. (2001). The global magnetic field of Mars and implications for crustal evolution. *Geophysical Research Letters*, *28*(21), 4015–4018.

Connerney, J. E. P., Espley, J., Lawton, P., Murphy, S., Odom, J., Oliversen, R., & Sheppard, D. (2015). The MAVEN magnetic field investigation. *Space Science Reviews*, *195*(1-4), 257–291.

Dehant, V., Lammer, H., Kulikov, Y. N., Grießmeier, J. M., Breuer, D., Verhoeven, O., & Lognonné, P. (2007). Planetary magnetic dynamo effect on atmospheric protection of early Earth and Mars. In *Geology and Habitability of Terrestrial Planets* (pp. 279–300). New York: Springer.

Frey, H. (2008). Ages of very large impact basins on Mars: Implications for the late heavy bombardment in the inner solar system. *Geophysical Research Letters*, *35*, L13203. https://doi.org/10.1029/2008GL033515

Gubbins, D., Ivers, D., Masterton, S. M., & Winch, D. E. (2011). Analysis of lithospheric magnetization in vector spherical harmonics. *Geophysical Journal International*, *187*, 99–117.

Hartmann, W. K. (2005). Martian cratering 8: Isochron refinement and the chronology of Mars. *Icarus*, *174*(2), 294–320.

Hartmann, W. K., & Neukum, G. (2001). Cratering chronology and the evolution of Mars. *Space Science Reviews*, *96*(1), 165–194.

Hood, L. L., Richmond, N. C., Pierazzo, E., & Rochette, P. (2003). Distribution of crustal magnetic fields on Mars: Shock effects of basin-forming impacts. *Geophysical Research Letters*, *30*(6), 1281. https://doi.org/10.1029/2002GL016657

Ivanov, B. A. (2001). Mars/Moon cratering rate ratio estimates. *Space Science Reviews*, *96*(1), 87–104.

Langel, R. A., & Hinze, W. J. (1998). *The magnetic fiel of the Earth's lithosphere: The satellite perspective*. Cambridge, UK: Cambridge University Press.

Langlais, B., & Thébault, E. (2011). Predicted and observed magnetic signatures of Martian (de) magnetized impact craters. *Icarus*, *212*(2), 568–578.

Langlais, B., & Purucker, M. (2007). A polar magnetic paleopole associated with Apollinaris Patera, Mars.*Planetary and Space Science*, *55*(3), 270–279.

Langlais, B., Purucker, M. E., & Mandea, M. (2004). Crustal magnetic field of Mars. *Journal of Geophysical Research*, *109*, E02008. https://doi.org/10.1029/2003JE002048

Lillis, R. J., Frey, H. V., & Manga, M. (2008). Rapid decrease in Martian crustal magnetization in the Noachian era: Implications for the dynamo and climate of early Mars. *Geophysical Research Letters*, *35*, L14203. https://doi.org/10.1029/2008GL034338

Lillis, R. J., Stewart, S. T., & Manga, M. (2013). Demagnetization by basin-forming impacts on early Mars: Contributions from shock, heat, and excavation. *Journal of Geophysical Research: Planets*, *118*, 1045–1062. https://doi.org/10.1002/jgre.20085

Lillis, R. J., Robbins, S., Manga, M., Halekas, J. S., & Frey, H. V. (2013). Time history of the Martian dynamo from crater magnetic field analysis. *Journal of Geophysical Research: Planets*, *118*, 1488–1511. https://doi.org/10.1002/jgre.20105

Lillis, R. J., Purucker, M. E., Halekas, J. S., Louzada, K. L., Stewart-Mukhopadhyay, S. T., Manga, M., & Frey, H. V. (2010). Study of impact demagnetization at Mars using Monte Carlo modeling and multiple altitude data. *Journal of Geophysical Research*, *115*, E07007. https://doi.org/10.1029/2009JE003556

Louzada, K. L., Stewart, S. T., Weiss, B. P., Gattacceca, J., Lillis, R. J., & Halekas, J. S. (2011). Impact demagnetization of the martian crust: Current knowledge and future directions. *Earth and Planetary Science Letters*, *305*(3), 257–269.

Milbury, C., & Schubert, G. (2010). Search for the global signature of the Martian dynamo. *Journal of Geophysical Research*, *115*, E10010. https://doi.org/10.1029/2010JE003617

Milbury, C., Schubert, G., Raymond, C. A., Smrekar, S. E., & Langlais, B. (2012). The history of Mars' dynamo as revealed by modeling magnetic anomalies near Tyrrhenus Mons and Syrtis Major. *Journal of Geophysical Research*, *117*, E1007. https://doi.org/10.1029/2012JE004099

Mohit, P. S., & Arkani-Hamed, J. (2004). Impact demagnetization of the Martian crust. *Icarus*, *168*(2), 305–317.

Morschhauser, A., Lesur, V., & Grott, M. (2014). A spherical harmonic model of the lithospheric magnetic field of Mars. *Journal of Geophysical Research: Planets*, *119*, 1162–1188. https://doi.org/10.1002/2013JE004555

Neukum, G. (1983). *Meteoritenbombardement und Datierung planetarer Oberflächen* (pp. 186). Munich, Germany: University of Munich.

Neumann, G. A., Zuber, M. T., Wieczorek, M. A., McGovern, P. J., Lemoine, F. G., & Smith, D. E. (2004). Crustal structure of Mars from gravity and topography. *Journal of Geophysical Research*, *109*, E08002. https://doi.org/10.1029/2004JE002262

Robbins, S. J., Hynek, B. M., Lillis, R. J., & Bottke, W. F. (2013). Large impact crater histories of Mars: The effect of different model crater age techniques. *Icarus*, *225*(1), 173–184.

Schubert, G., Russell, C. T., & Moore, W. B. (2000). Geophysics: Timing of the Martian dynamo. *Nature*, *408*, 666–667.

Shahnas, H., & Arkani-Hamed, J. (2007). Viscous and impact demagnetization of Martian crust. *Journal of Geophysical Research*, *112*, E02009. https://doi.org/10.1029/2005JE002424

Shuster, D. L., & Weiss, B. P. (2005). Martian surface paleotemperatures from thermochronology of meteorites. *Science*, *309*(5734), 594–600.

Smith, D. E., Zuber, M. T., Frey, H. V., Garvin, J. B., Head, J. W., Muhleman, D. O., & Banerdt, W. B. (2001). Mars Orbiter Laser Altimeter: Experiment summary after the first year of global mapping of Mars. *Journal of Geophysical Research*, *106*(E10), 23,689–23,722.

Solomon, S. C., Aharonson, O., Aurnou, J. M., Banerdt, W. B., Carr, M. H., Dombard, A. J., & Jakosky, B. M. (2005). New perspectives on ancient Mars. *Science*, *307*, 1214–1220.

Stevenson, D. J. (2001). Mars' core and magnetism. *Nature*, *412*, 214–219.
Stewart, A. J., Schmidt, M. W., van Westrenen, W., & Liebske, C. (2007). Mars: A new core-crystallization regime. *Science*, *316*(5829), 1323–1325.
Vervelidou, F., Lesur, V., Morschhauser, A., Grott, M., & Thomas, P. (2017). On the accuracy of palaeopole estimations from magnetic field measurements. *Geophysical Journal International*, *211*, 1669–1678. https://doi.org/10.1093/gji/ggx400
Vilim, R., Stanley, S., & Hauck, S. A. (2010). Iron snow zones as a mechanism for generating Mercury's weak observed magnetic field. *Journal of Geophysical Research*, *115*, E11003. https://doi.org/10.1029/2009JE003528
Voorhies, C. V. (2008). Thickness of the magnetic crust of Mars. *Journal of Geophysical Research*, *113*, E04004. https://doi.org/10.1029/2007JE002928
Weiss, B. P., Shuster, D. L., & Stewart, S. T. (2002). Temperatures on Mars from $^{40}Ar/^{39}Ar$ thermochronology of ALH84001. *Earth and Planetary Science Letters*, *201*(3), 465–472.
Weiss, B. P., Vali, H., Baudenbacher, F. J., Kirschvink, J. L., Stewart, S. T., & Shuster, D. L. (2002). Records of an ancient Martian magnetic field in ALH84001. *Earth and Planetary Science Letters*, *201*(3), 449–463.
Werner, S. C. (2008). The early Martian evolution—Constraints from basin formation ages. *Icarus*, *195*(1), 45–60.
Werner, S. C. (2014). Moon, Mars, Mercury: Basin formation ages and implications for the maximum surface age and the migration of gaseous planets. *Earth and Planetary Science Letters*, *400*, 54–65.
Werner, S. C., Ody, A., & Poulet, F. (2014). The source crater of Martian shergottite meteorites. *Science*, *343*(6177), 1343–1346.
Whaler, K. A., & Purucker, M. E. (2005). A spatially continuous magnetization model for Mars. *Journal of Geophysical Research*, *110*, E09001. https://doi.org/10.1029/2004JE002393